Electron Bernstein Wave Heating and Emission in the TCV Tokamak

A. Mueck [1], *Y. Camenen* [1], *S. Coda* [1], *L. Curchod* [1], *T.P. Goodman* [1], *H.P. Laqua* [2], *A. Pochelon* [1], *L. Porte*[1], *V.S. Udintsev*[1], *F. Volpe*[2], *TCV Team* [1]

[1]Ecole Polytechnique Fédérale de Lausanne EPFL, Centre de Recherches en Physique des Plasmas, Association EURATOM- Confédération Suisse, 1015 Lausanne

[2]Max-Planck-Institut für Plasmaphysik, EURATOM Assoziation, D-17491 Greifswald

Mail to: Anja.mueck@ipp.mpg.de

Fax: 0049-89-3299 1313

Pages: 30

Figures: 16

Tables: none

ABSTRACT

Electron Cyclotron Resonance Heating (ECRH) of high density tokamak plasmas is limited due to reflections of the waves at so-called wave cut-offs. Electron Bernstein Wave Heating (EBWH) via a double mode conversion process from ordinary (O) mode, launched from the low field side, to extraordinary (X) and finally to Bernstein (B) mode offers the possibility to overcome these density limits.

In this article, the O-X mode conversion dependence on the microwave injection angle is demonstrated experimentally. The dependence on the injection angle is studied in high density plasmas in H-mode, in presence of magnetohydrodynamic activity, edge localized modes (ELMs) and sawteeth. Results of localized heat deposition at an overdense location are presented, demonstrating EBWH for the first time via the O-X-B mode conversion process in a standard aspect-ratio tokamak. The results of global and local power deposition are compared with ray tracing calculations. Moreover, a temperature increase due to EBWH is observed.

Initial Electron Bernstein wave Emission (EBE) measurements with a newly installed ECRH reception launcher are presented. The inverse double mode conversion process B-X-O is observed by measuring the emission for several frequencies at an optimum angle.

INTRODUCTION

In a tokamak reactor, the fusion reaction rate and the energy confinement increases with the plasma density. However, the heating of high density plasmas with Electron Cyclotron Resonance Heating (ECRH) is limited by the reflection of the microwaves at so-called wave cut-offs before the energy is deposited in the core plasma [1]. The double mode conversion scheme from O-mode to X-mode and finally to Bernstein mode (O-X-B) offers the possibility to overcome this limitation [2, 3]. The Bernstein mode has no density cut-off in the plasma, but cannot propagate in vacuum and has therefore to be excited by mode conversion. For a certain injection angle, the quasi-circular polarized O-mode wave converts at the plasma cut-off into the X-mode and propagates back to the upper hybrid resonance. Close to this resonance, the X-mode is converted into the electrostatic Bernstein mode, which propagates towards the plasma center and is absorbed at harmonics of the cyclotron resonance. In a hot plasma, this second conversion occurs with a near 100% efficiency. The power transmission function T for the O- to X-mode conversion was derived by Mjølhus [4] and defines the angular window for the O-X conversion

$$T(N_\perp,N_\parallel)=\exp(-\pi k_0 \mathbf{L_n}(Y/2)^{1/2}[2(1+Y)(\mathbf{N_{\parallel,opt}}-\mathbf{N_\parallel})^2+N_\perp^2]) \qquad (1)$$

with the density-gradient scale length $L_n=n_e/(\partial n_e/\partial x)$, the perpendicular and parallel refraction indices to the magnetic field $N_\perp$, $N_\parallel$ and with $Y = \omega_{ce}/\omega$ where ω_{ce} is the electron cyclotron frequency. Only for the optimum parallel refraction index $N_{\parallel,opt}^2=Y/(Y+1)$, equivalent to an optimum injection angle, the O-mode wave can be completely converted to X-mode. The fraction of the radiation that is not mode converted is reflected back towards the plasma edge and either escapes the device or is absorbed via multi-pass absorption.

Electron Bernstein Wave Heating (EBWH) via this O-X-B double mode conversion scheme was successfully demonstrated in the stellarator W7-AS [5], in the High Density High confinement (HDH) mode. Electron Bernstein Emission (EBE)

measurements in spherical, low aspect-ratio tokamaks and in reversed field pinches are reported [6-8]. The work presented here demonstrates electron Bernstein wave heating for the first time in a classical aspect-ratio tokamak and electron Bernstein wave emission measurements.

TCV AND THE TARGET PLASMA

In the Tokamak à Configuration Variable (TCV) the main heating source relies on ECRH at the second harmonic frequency 82.7 GHz, see Figure 1. The power of six gyrotrons, delivering 500 kW each, is injected through launchers from four upper lateral and two equatorial ports. The launcher mirrors can be steered in real time in two dimensions. The resulting beam direction is parameterized by two launcher angles, which will henceforth be termed the poloidal and toroidal angles. Reflected EC power, not absorbed by the plasma, is assessed by measuring the EC stray radiation level via semiconductor diodes, installed in several sectors of TCV. At a standard TCV magnetic field of B = 1.5 T, the plasma becomes overdense to the second harmonic X-mode for electron densities of $n_e \sim 4.2 \cdot 10^{19}$ m^{-3} and to the O-mode at $n_e \sim 8.7 \cdot 10^{19}$ m^{-3}.

To achieve a large angular window of the power transmission function, the density scale length at the plasma cut-off has to be short, requiring a steep density gradient, see equation 1. This condition is fulfilled in TCV H-modes [9] with central electron densities of $n_e \geq 1 \cdot 10^{20}$ m^{-3} and magnetohydrodynamic activity like ELMs and sawteeth. At these densities, the plasma cut-off is placed at $\rho_\psi \sim 0.9$, at the steep edge density gradient region of the H-mode. The high densities are achieved in non-stationary conditions with alternating ELMy and ELM-free phases. In Figure 2, the temporal evolution of a typical target plasma is shown. The coupled density and density gradient rise during the ELM-free phases and drop with the onset of an ELMy phase. To avoid a perturbation of the H-mode, EC power of 500 kW was injected with a low duty cycle of 6%. The stray radiation level, shown in Figure 2, mainly decreases with increasing density. The decrease in the stray level, equivalent with an increase of

the EC power absorption, and the increase in the density gradient lead to a broader angular window for the O-X mode conversion, see equation 1. The stray level increases rapidly just after an ELM, indicating that less EC power is absorbed, due to the resulting drop in the density and the density gradient induced by the ELMs, shown in more detail in the D_α time traces in Figure 3.

EXPERIMENTAL DETERMINATION OF OPTIMUM ANGLE

As a first step, single ray simulations with the non-relativistic ART ray tracing code [10, 11] including O-X-B mode conversion for wave propagation and absorption was performed for the target plasma conditions, allowing the determination of the optimum injection angles.

Around this pair of calculated optimum angles, poloidal and toroidal angle scans were performed to experimentally obtain the optimum injection angles. As shown in Figure 4a and b, clear minima in the stray radiation level are measured, indicating maxima of power absorption, thus determining the measured optimum angle to a poloidal angle of about 31° and a toroidal angle of about 112°. A comparable angle dependence in the stray radiation is found for both upper lateral and equatorial launch in all stray diode signals, measured at various positions in the torus.

The experimentally determined optimum angles are compared with the results of the simulation with the ART ray tracing code. In Figure 5, the simulated O-X conversion efficiency is shown in a contour plot of the poloidal launcher angle over the toroidal launcher angle. The innermost contour indicates 90% conversion, the outermost contour 10%. The experimental angles of the poloidal and the toroidal scans for an equatorial launch are added as violet dots and the extrapolated optimum angle as a green dot. This experimental optimum angle is in agreement with the simulated angle within 3°.

This small discrepancy can be explained by the resolution of the scans and the imprecision of the magnetic equilibrium reconstruction of ~ ±1 cm. When such a variation is applied to the ART simulation, the optimum angle varies by ~ ±1°.

In Figure 6, a comparison between the angular windows of the measured stray level in percent and of the ART simulation is shown. The simulated percentage of the O-X conversion is taken from Figure 5 for the same angles as used in the experimental scans. The discrepancy between the measured and calculated angular window is not surprising in view of the finite width of the EC beam and the spread in its wave-number spectrum, which is expected to broaden the width of the conversion efficiency function as well as to reduce its absolute value. This last point is consistent with the non-zero measured minimum stray level, indicating that less than 100% of the beam power are absorbed.

Both the angle dependence and the good agreement of the optimum angles, determined in the experiments and simulations, strongly indicate a successful O-X-B mode conversion [12-15].

GLOBAL AND LOCAL BERNSTEIN WAVE HEATING

Heating experiments were performed after the experimental determination of the optimum angles. The duty cycle was increased to 46% and ~ 500 kW EC power injected with a modulation frequency of 182 Hz at the optimum angle. The modulation frequency was chosen between the first harmonic of the sawtooth instability at ~ 110 Hz and its second harmonic.

A basic cross-check of the O-X transmission can be performed simply by comparing the stray radiation levels when power is injected in the vicinity of the optimum angles in O- and X-mode. Figure 7 shows the stray radiation levels when injecting alternatively O- and X-mode in an ELM-free phase with the same EC power of ~ 500 kW. The stray level for O-mode injection is indeed only 40% of the X-mode stray level, indicating much higher absorption with O-mode than with X-mode.

The overall globally absorbed power can be measured with the diamagnetic loop [16], measuring the toroidal magnetic flux variation, which is related to the plasma stored energy. An absorption of typically 60% is observed for O-mode injection, as shown in Figure 8. In X-mode, the absorption remains below 10%, indicating that the O-mode can penetrate into the plasma while the X-mode is reflected, as expected for overdense

plasmas. A total power absorption measurement cannot conclusively prove the nature of the absorption mechanism, which can also involve edge absorption of waves generated by nonlinear wave-wave coupling as well as absorption of waves multiply reflected on the vacuum vessel. In addition to the angle dependence demonstrated in the previous section, a determination of the power deposition location is therefore essential to prove heating via EBW.

The plasma center of the high density target plasma is strongly affected by the sawtooth instability, which regularly leads to the ejection of the hot plasma core towards the colder edge region. In the core of the plasma, close to this dominating instability, the proof of power deposition due to EBWH is very difficult. Therefore, conditions for a deposition location away from the plasma core, but well inside the plasma cut-off were chosen. In Figure 9, an ART simulation of such a wave path is shown in the poloidal and toroidal projections. The O-mode wave propagates to the plasma cut-off, is converted into X-mode and continues its path back to the upper hybrid resonance, where it is converted into Bernstein mode. Then the Bernstein wave propagates towardsthe plasma center and is absorbed at $\rho_\psi \sim 0.78$, well inside the plasma cut-off layer at $\rho_\psi \sim 0.9$ (see Figure 11b)).

The deposition location is determined experimentally by inspecting soft X-ray time traces, measured by a multi-wire proportional detector, covering the entire plasma cross section with its 64 lines of sights in the vertical direction [17]. The soft X-ray emissivity has a monotonically increasing dependence on the electron temperature and the plasma density. In Figure 10, as the plasma density increases monotonically, the modulation of the soft X-ray emissivity, visible in the line integrated time traces of several channels, on both the High Field Side (HFS) and Low Field Side (LFS) can be attributed to the modulation of the temperature caused by modulated ECRH. To determine the ECRH power deposition location, an FFT analysis of each of the 64 soft X-ray chords was performed. The FFT amplitude of the peak at the ECRH modulation frequency is plotted over the soft X-ray channel number in Figure 11a. Two clear maxima in the amplitude are visible. These broad spatial peaks correspond to chords to $\rho_\psi \sim 0.65$, on both HFS and LFS. The maximum on the HFS is more pronounced

due to the effects of line integration and plasma triangularity, causing such an asymmetry.

Since the soft X-ray chords are line integrated, an integral inversion is necessary to derive the local emissivity distribution. This is accomplished under the assumption of a poloidally constant emissivity and by employing a Fisher regularization algorithm. In Figure 11b, the FFT amplitude of the inverted data at the EC modulation frequency is represented as a function of the poloidal flux coordinate ρ_ψ. The peak of the FFT amplitude after the inversion is located at $\rho_\psi \sim 0.7$. This experimental peak deposition location is close to the calculated one at $\rho_\psi \sim 0.78$, within only 10%. The slight difference may be attributed again to uncertainties in the equilibrium reconstruction and in the density gradient measurement.

However, the good agreement of the theoretical and experimental deposition locations together with a deposition of the heating power inside the plasma cut-off constitutes a strong proof that the O-X-B mechanism is at play and that the plasma is heated by EBWH.

CENTRAL ELECTRON TEMPERATURE INCREASE BY ELECTRON BERNSTEIN WAVE HEATING

To be able to observe an increase of the central temperature over several confinement times, the injected power was increased to 1 MW and the pulse length to 100 ms, as shown in Figure 12. The magnetic field and the injection angles are chosen such that both upper lateral and equatorial launchers heat at the same location at $\rho_\psi \sim 0.4$ (calculated with ART). The central temperature evolution, shown in Figure 12, is measured via the soft X-ray absorber method. TCV is equipped with 3 soft X-ray cameras, equipped with different beryllium thicknesses to measure the electron temperature. All of them show the same behaviour: an increase of the temperature $\Delta T_e \sim 80$ eV during the EC pulse. During the heating pulse, the density remains quasi-constant, which emphasizes that the temperature evolution is essentially the result of EBWH. The measurement of this temperature increase is supported by Thomson

scattering measurements. Figure 13 shows two Thomson temperature profile fits, one at 1.0 s before the EC pulse and one at 1.1 s during the EC pulse. An increase of the central temperature is also observed, supporting the temperature measurements with the soft X-ray absorber method.

ELECTRON BERNSTEIN WAVE EMISSION MEASUREMENTS

Initial Electron Bernstein Emission measurements were performed in plasmas with reversed magnetic field and current with a newly installed equatorial launcher with steerable mirrors. This refurbished launcher is similar in geometry to the other six launchers connected to the gyrotrons, but is only meant to be used for reception measurements. It is attached to the LFS ECE system via a several meters long open-ended over-moded 1 inch diameter waveguide line, connected to a switch at the radiometer side, after being downtapered and converted to a fundamental waveguide with a rectangular cross section. The transmission line was optimized to observe modes with a vertical polarization (approximately X-mode, when viewing perpendicularly), without additional polarizer. Since the oblique O-mode is quasi-circularily polarized, the difference in the measurement of horizontal or vertical (linear) polarization is low.

Via the radiometer, emission with frequencies ranging fom 65 to 110 GHz can be observed. As in the previously described heating experiments, the optimum angle was first determined with the ART code. Then, poloidal and toroidal angle scans on a shot to shot basis were performed to determine experimentally the optimum angle. In Figure 14, first EBE measurements close to the optimum angle are presented for several frequencies. A clear emission signal is observed on all channels for an overdense plasma. The emission signals show also a clear maximum in the reception angle, comparable to the minimum in the stray signal with modulated EC injection, as described in the previous sections. The emission signal drops with the appearance of ELMs in a similar way than the stray signal increases during ELMs, pointing out the dependence of both processes on the profiles. This indicates that the two mechanisms are indeed due to EBE and EBWH.

For the different frequencies, the onset of the overdense emission signal is dependent on the density. The onset density increases with the frequency, as expected, and is comparable to the cut-off density. In Figure 15, the calculated cut-off densities for various frequencies are compared with a high temporal resolution line-integrated density measurement (FIR) and the Thomson density on axis. The measured EBE onset densities are in good agreement with the calculated cut-off densities and differ only by 5-10%.

The same experiment was performed for horizonal polarization (pure O-mode). As expected, a similar result was obtained with the emission signal being slightly higher by 20%.

As shown in polar diagrams of the CMA diagram [1], the O-mode couples to the left hand circularly polarized mode (L-mode), dependent on the injection angle; meaning that an oblique O-mode wave is left-hand quasi-circularly polarized. By inserting a polarizer (circular-linear), a mode with one handiness can be selected. Figure 16 shows two discharges close to the optimum angles with the selection of opposite handinesses. As expected, the overdense emission is only observed for one handiness, so it can be concluded, that the mode is quasi-circularly polarized, as expected for oblique O-mode.

In summary, the emission is dependent on the emission angle and is observed above a density threshold. The threshold differs for the different frequencies and corresponds to the cut-off densities. The emission signal is stronger for horizontal O-mode than for vertical polarization (X-mode) and has a well defined handiness. Therefore, there is strong evidence that the observed emission is actually Electron Bernstein Emission (EBE).

CONCLUSIONS AND OUTLOOK

In conclusion, the first demonstration of EBW heating by O-X-B double mode conversion in an overdense conventional aspect-ratio tokamak has been obtained in the TCV device.

The optimum injection angle for O-X-B conversion was demonstrated experimentally by 2D angle scans via microwave stray radiation measurements in discharges with modulated EC wave injection at a low duty cycle. Ray tracing simulations with the ART code were performed yielding an optimum angle in good agreement with the measurements.

Higher duty cycle modulated EC waves were injected to perform bulk EBWH.

An average absorbed power fraction of about 60 % was measured with densities well above the cut-off. The spatial distribution of the power absorption was determined experimentally by FFT analysis of soft X-ray emissivity from a high spatial resolution camera. The local deposition was found to be well inside the plasma cut-off and matches the value predicted by ART within the experimental uncertainties.

To measure a temperature increase, the injection angle and the magnetic field were adjusted to achieve more central absorption. A central temperature increase was measured consistently by Thomson scattering and the soft X-ray absorber method.

Initial electron Bernstein wave emission measurements were presented, reproducing the calculated cut-off density at the EBE onset for several frequencies. The emission is higher for horizontal than for vertical polarization and has a well defined handiness. Therefore, there is strong evidence that the observed emission is dominated by electron Bernstein wave emission.

In summary, localized heating experiments were presented, demonstrating EBWH for the first time via the O-X-B mode conversion process in a standard aspect-ratio tokamak.

ACKNOWLEDGMENTS

The ART software has been acquired with kind permission of IPP-Garching. This work is partly funded by the 'Fonds National Suisse pour la recherche scientifique'. The Author A. Mueck is supported by a EURATOM Fusion fellowship.

FIGURES

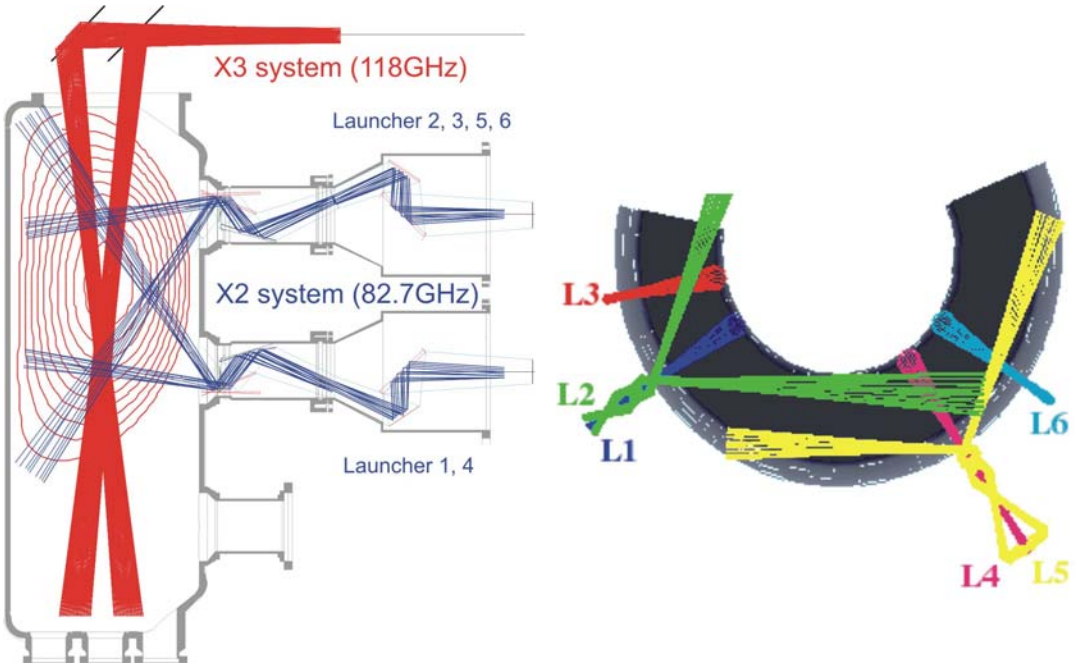

Figure 1: The ECRH system of TCV heats the plasma at the second harmonic with six gyrotrons at 82.7 GHz and a power of 500kW each. The waves are injected by four upper lateral launchers and two equatorial launchers which can be rotated in two directions.

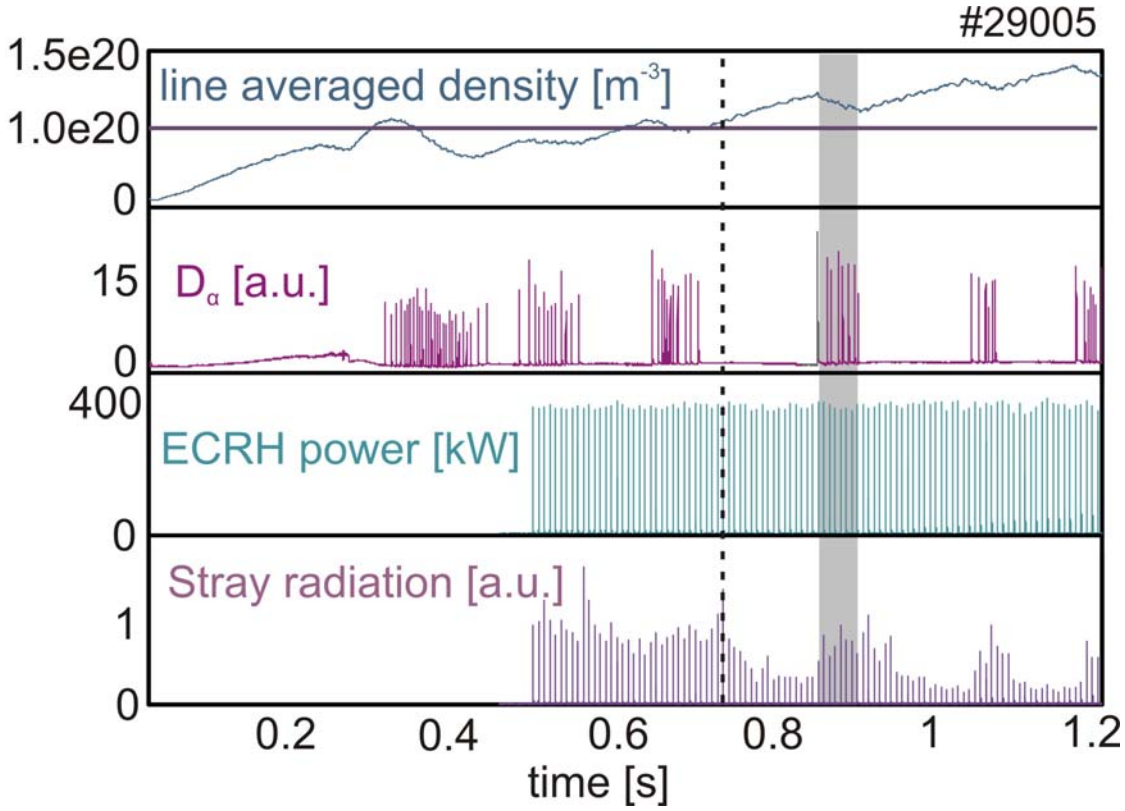

Figure 2: Typical target plasma: high density ELMy H-mode with ELM-free phases. Modulated EC waves are injected in O-mode. When the plasma becomes overdense, the stray level is low in the ELM-free phases and increases in the ELMy phases, as shown in the highlighted region.

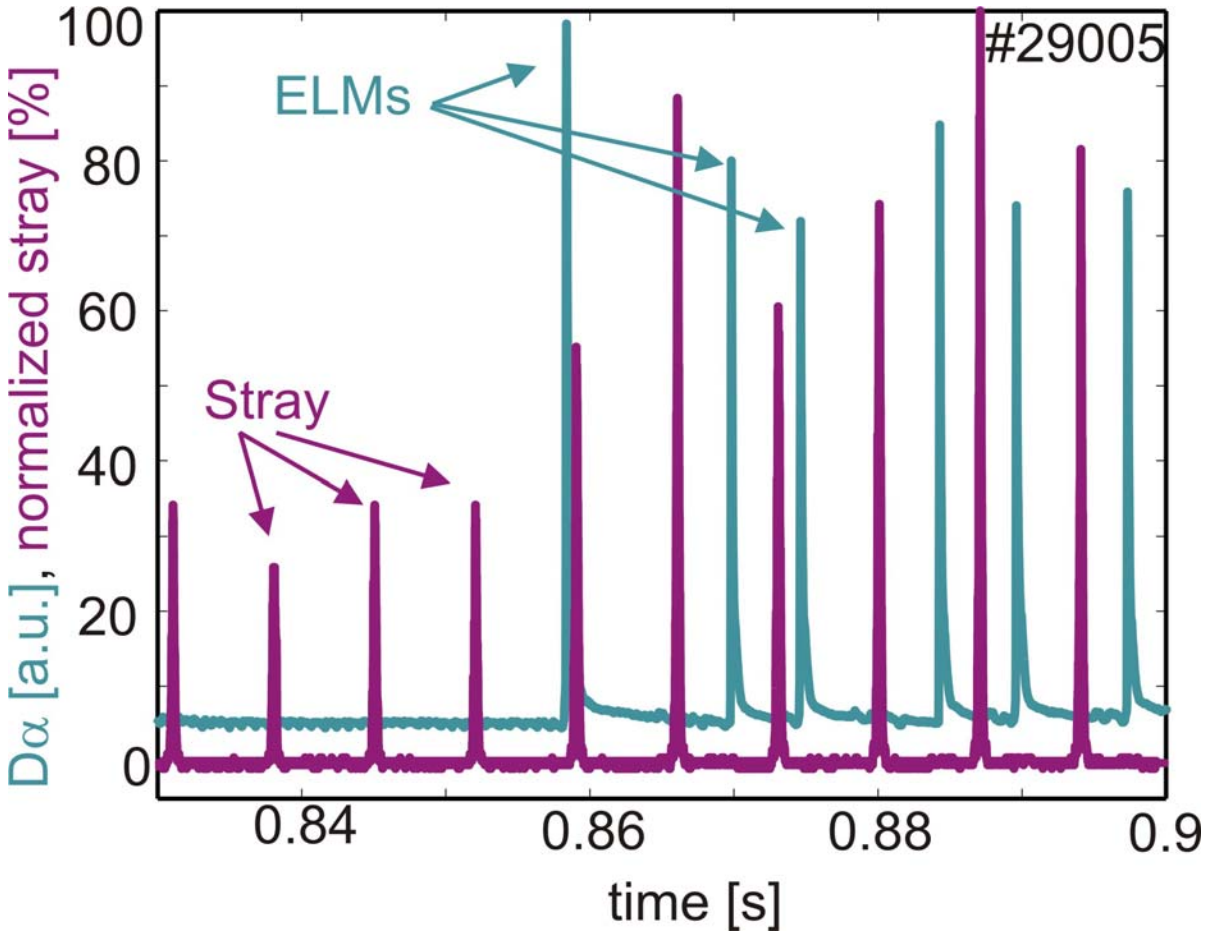

Figure 3: Normalized stray radiation power (violet) and D_α light emission (green). ELMs can strongly influence the stray radiation. The stray power, measured during the short EC pulses, rises from 30% to 80% during an ELMy phase.

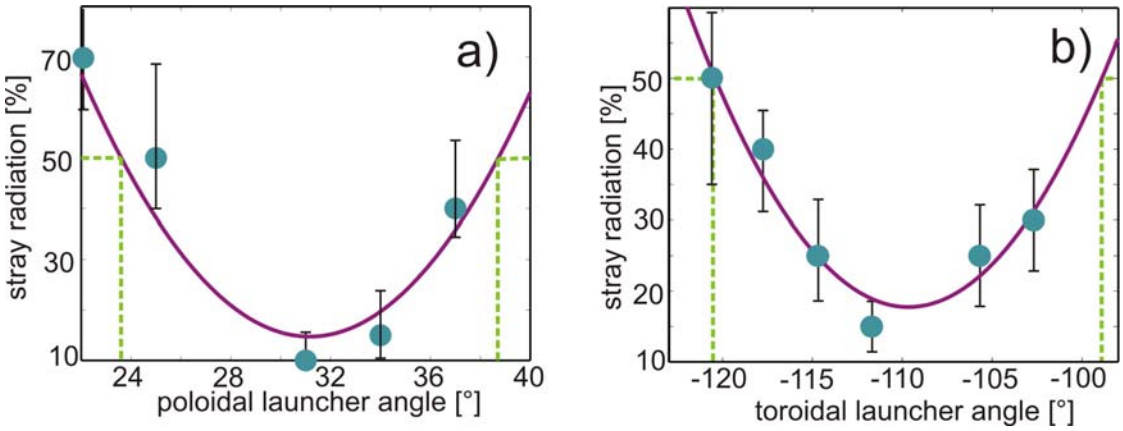

Figure 4: Normalized stray radiation power vs. a) poloidal angle (with constant toroidal angle) and b) toroidal angle (with constant toroidal angle). The solid curves represent polynomial regression fits to the data points, the dashed lines represent 50% of the maximum stray level. A clear minimum in the stray radiation level is found for both angle scans.

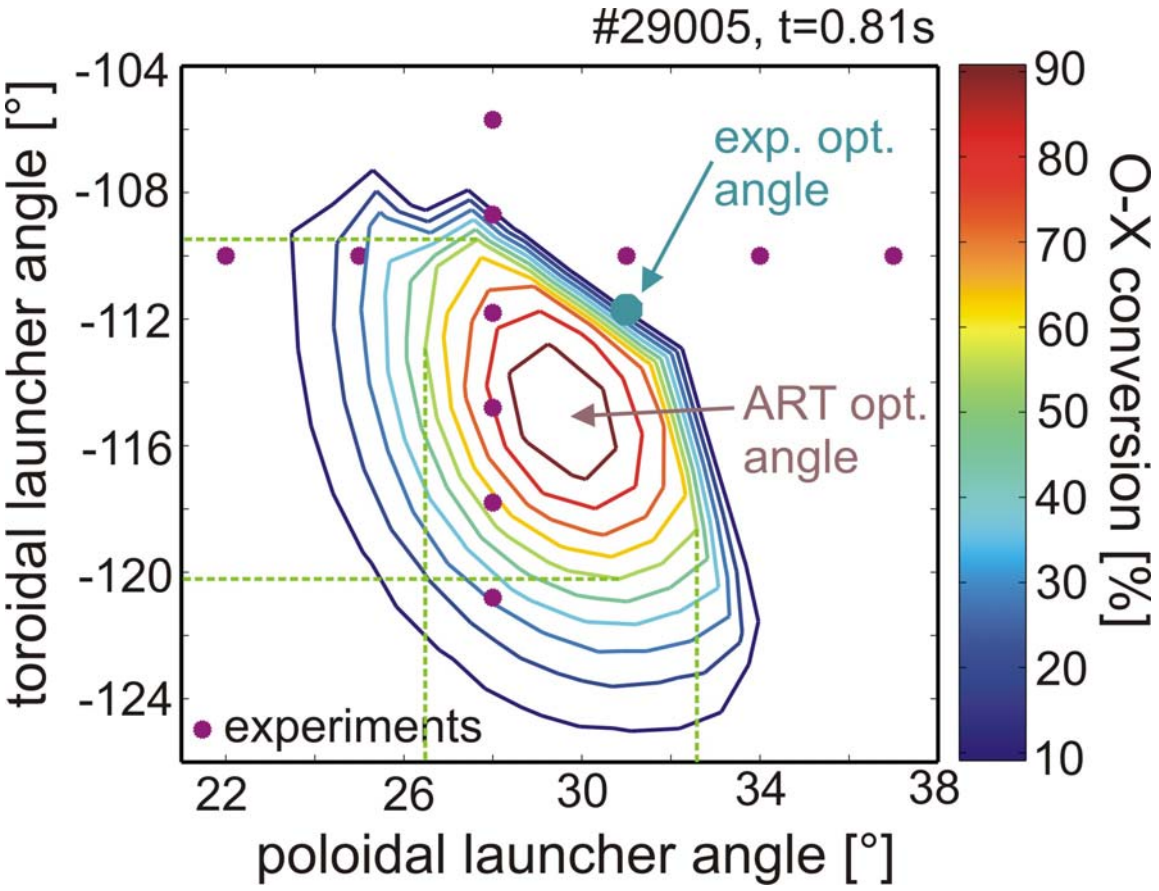

Figure 5: Contour plot of calculated O-X conversion efficiency vs. launching angles. The innermost contour indicates 90% O-X conversion, the outermost 10%. The dashed lines denote the minimum and maximum angles of the 50% conversion window. The superimposed points give the angles of the experimental scans (see Figure 4). The green point corresponds to the extrapolated optimum experimental angles and is within 3° of the calculated angles.

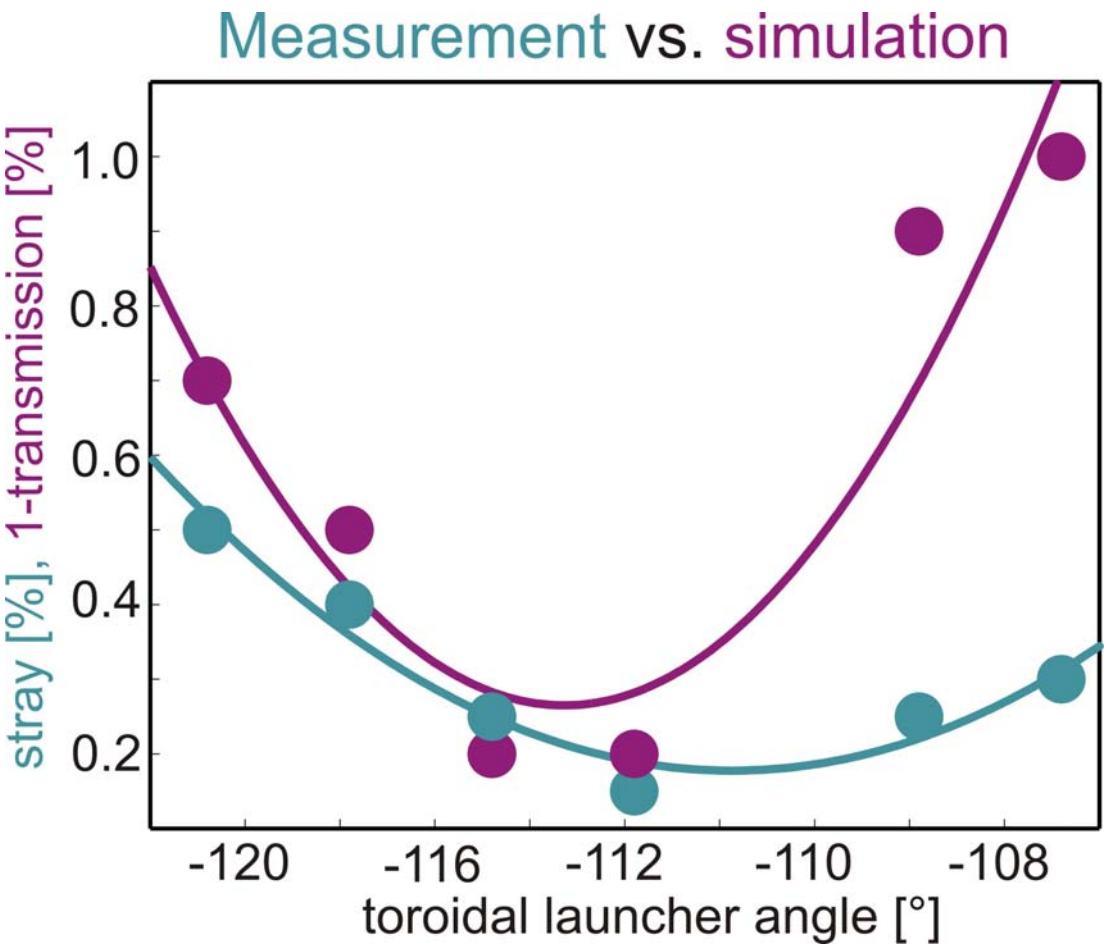

Figure 6: Comparison of experimental (see Figure 4b) and simulated angular window.

The experimental angular width is significantly broader than the simulated one, but can be explained by the finite width of the EC beam and the spread in its wave number spectrum.

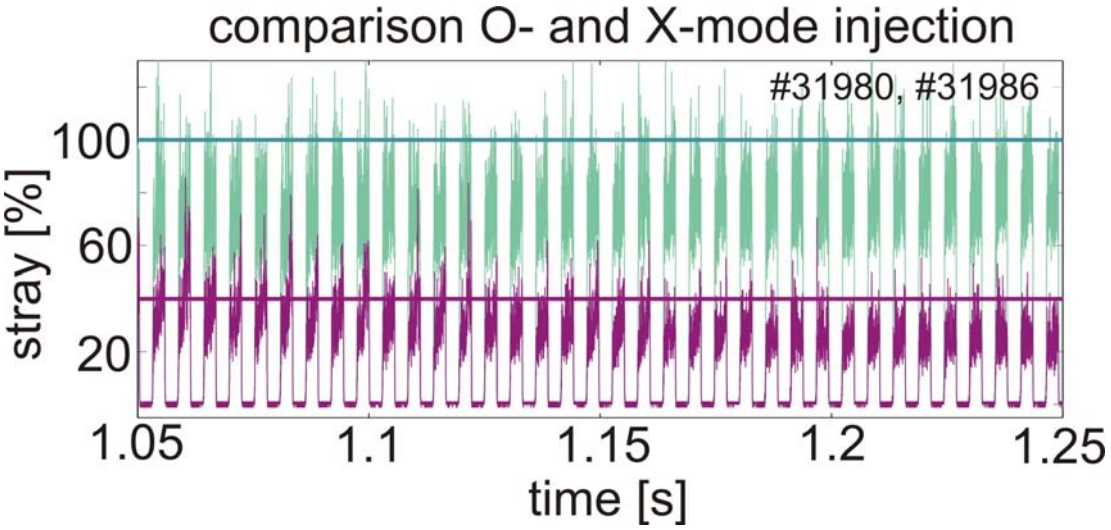

Figure 7: Stray radiation for O- (violet) and X-mode (green) injection during an ELM-free period for identical injection angles and plasma conditions. In O-mode, the stray level is only about 40% of the stray level in X-mode.

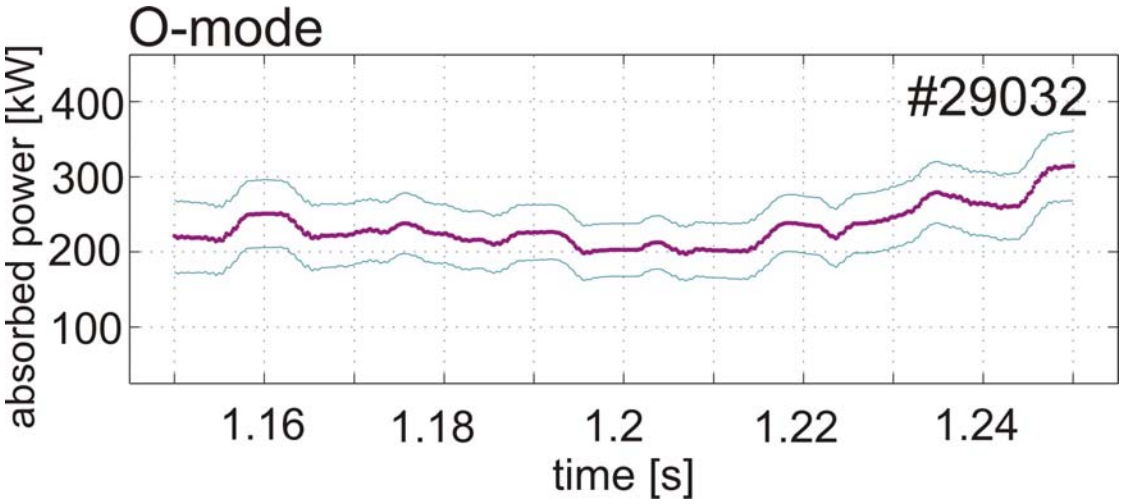

Figure 8: Average deposited power from experiment with modulated EC wave injection, determined with the diamagnetic flux loop diagnostic. The absorbed power is about 60% of the injected EC power.

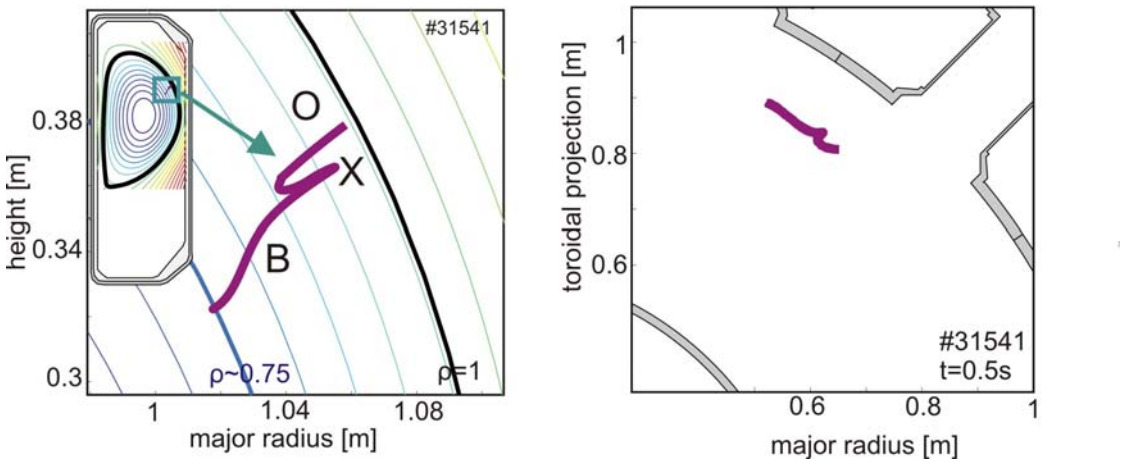

Figure 9: ART ray tracing calculation of the wave path in the a) poloidal and b) toroidal projections, including O-X-B double mode conversion.

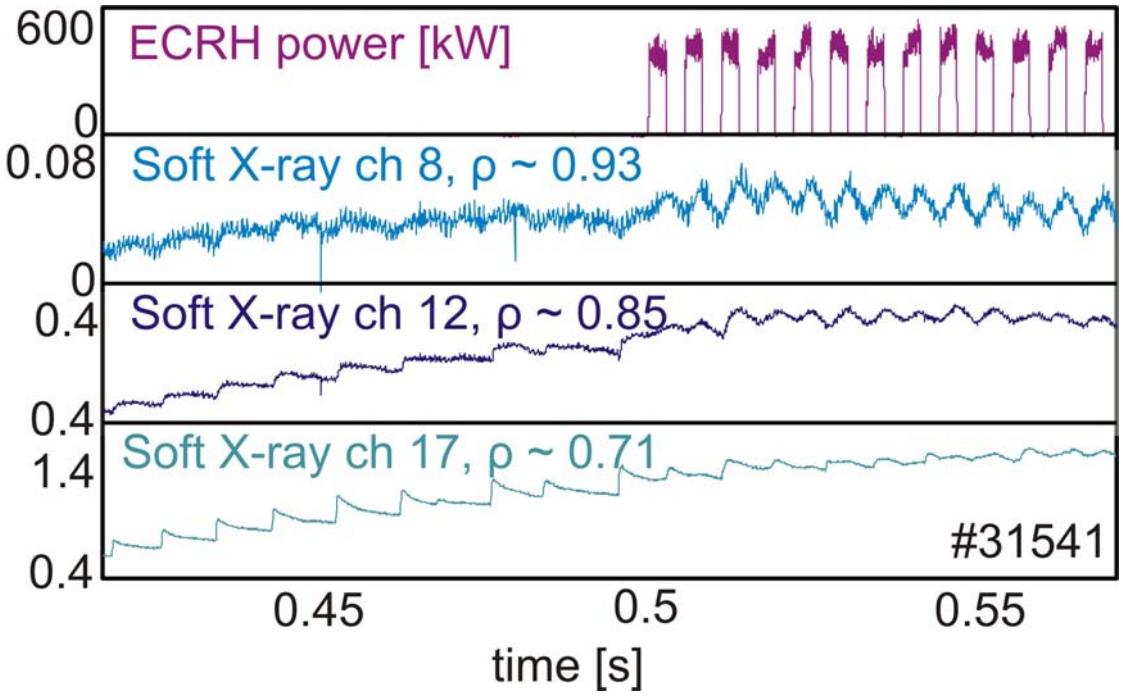

Figure 10: The injection of modulated EC waves is visible directly on several radial soft X-ray time traces. To determine the deposition location, an FFT of each channel is performed.

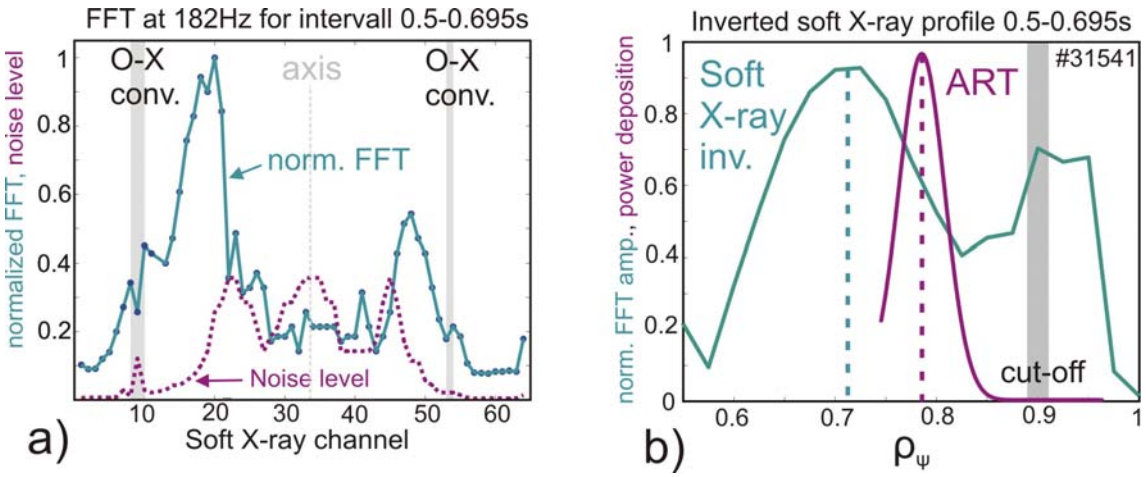

Figure 11: a) Normalized FFT amplitude of the line-integrated soft X-ray time traces at the modulation frequency of the injected EC waves at 182 Hz vs. the chord number (green). The noise level is shown for reference (violet). b) Local soft X-ray emissivity oscillation amplitudes at the modulation frequency, derived by integral inversion from the line-integrated soft X-ray chords (green) and normalized density of the deposited beam power, calculated with ART. The power is absorbed well inside the cut-off at $\rho_\psi \sim 0.78$.

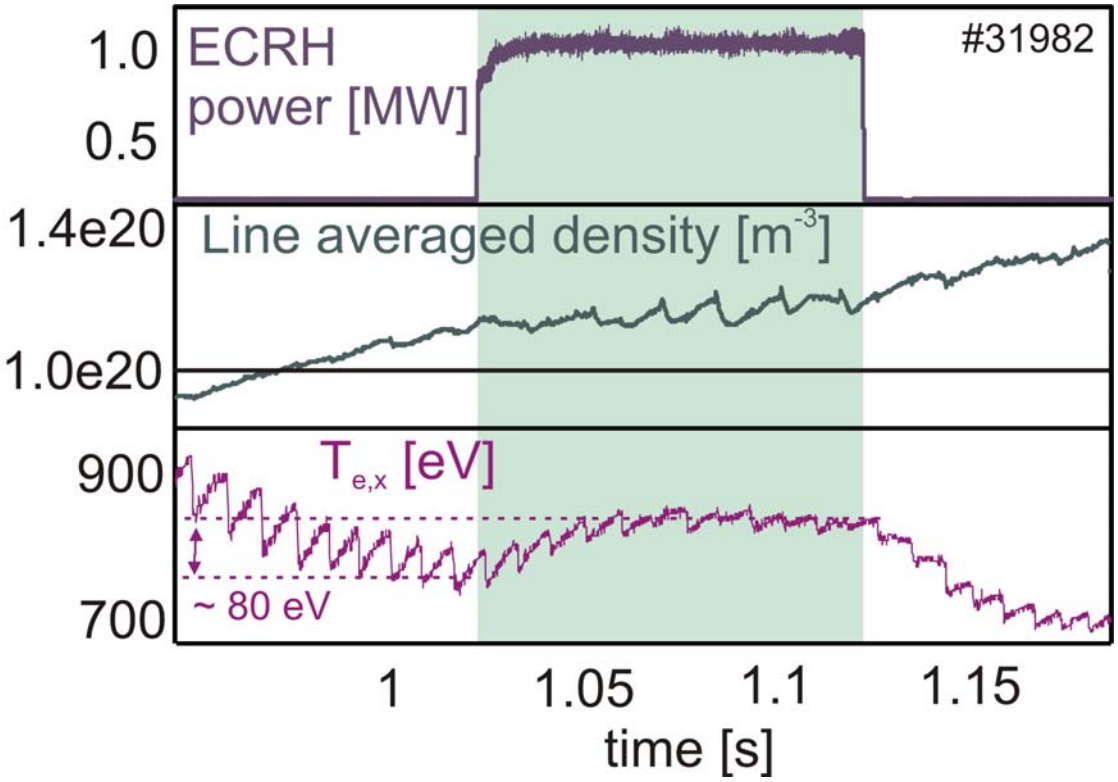

Figure 12: The long EC power pulses of 100 ms were injected to be able to show a temperature increase due to EBWH. A clear increase in the temperature, measured by the soft X-ray absorber method is shown. The density remains essentially constant, which allows to attribute the temperature increase to EBWH (P_{Ohm} = 0.6 MW, P_{ECRH} = 1 MW and additional P_{ECRH} = 1 MW pulses of 100 ms).

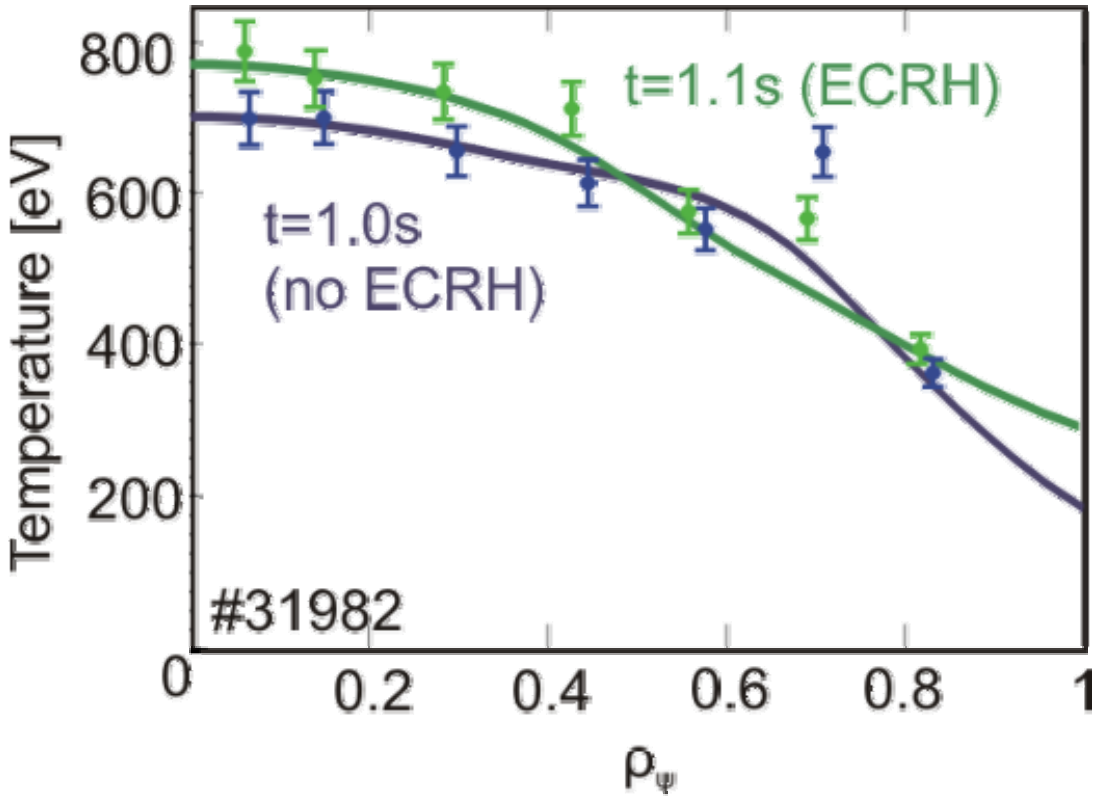

Figure 13: Temperature profiles before the EC power pulse (1.0 s) and during the EC pulse (1.1 s), measured with Thomson scattering. The central temperature increase measured by Thomson scattering confirms the soft X-ray temperature measurement.

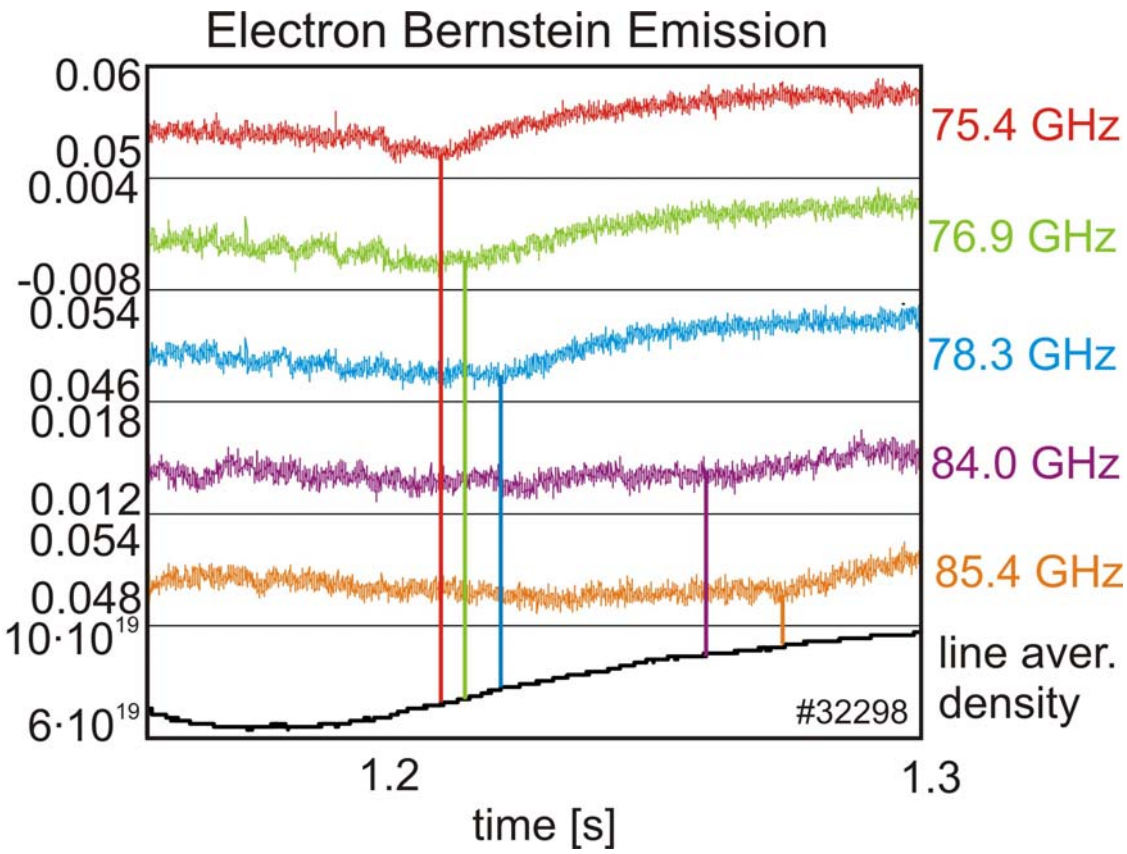

Figure 14: The emission at overdense conditions is measured at several frequencies. The onset of this emission varies with the density for the different frequencies, as expected. The onset densities correspond to the calculated cut-off densities within 5-10% for the various frequencies.

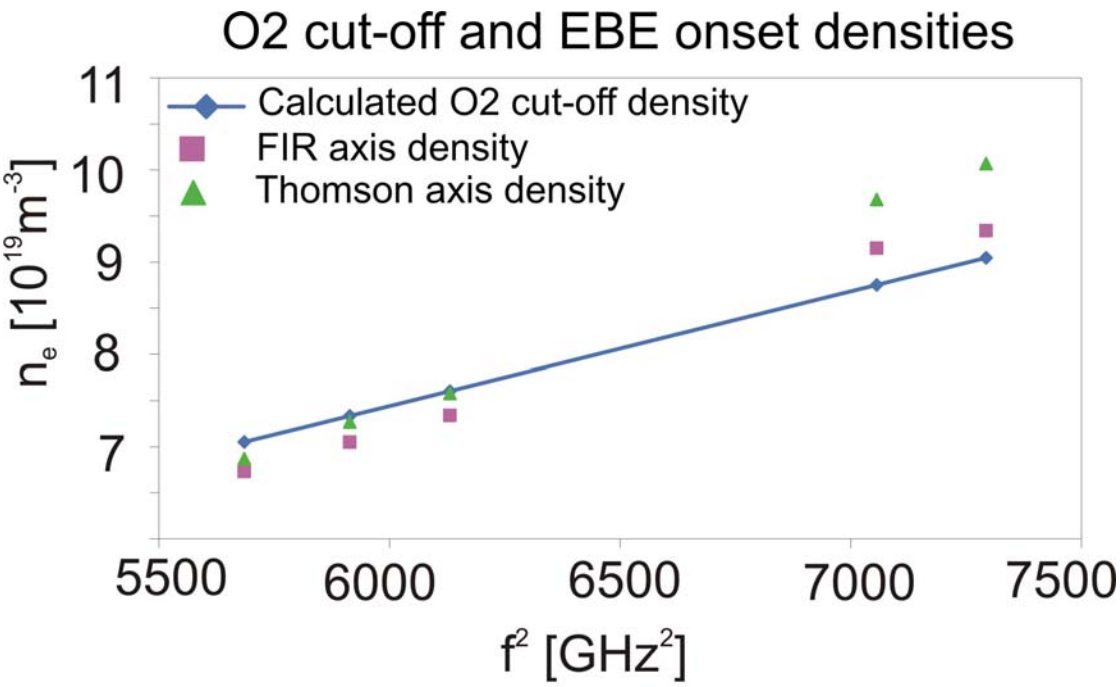

Figure 15: Comparison between calculated O-mode cut-off densities, the measured density from the FIR high time resolution line averaged density reconstruction and Thomson density measurement on axis for the square of several frequencies. A clear dependence with a deviation of less than 10% is shown.

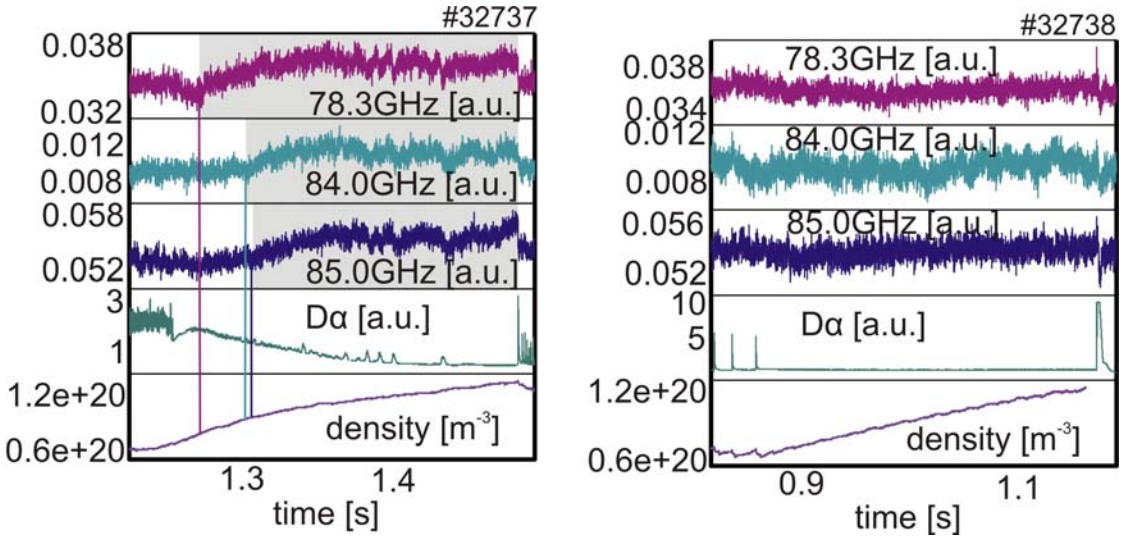

Figure 16: Similar discharge as in Figure 14 but with a polarizer included to differ between opposite polarisation handinesses. The overdense emission signal is observed for only one handiness in ELM-free phases.

REFERENCES

1. T.H. Stix, Waves in Plasmas, Springer Verlag New York, Inc., 1992
2. I. Bernstein, Phys. Rev. Lett. **109**, 10 (1958)
3. J. Preinhaelter, V.Kopecky, J. Plasma Physics **10**, part 1 (1973), pp 1-12
4. E. Mjølhus, J. Plasma Phys**. 31**, 7 (1984)
5. H.P. Laqua et al., Phys. Rev. Lett. **78**, 3467 (1997)
6. V. Shevchenko et al., 15th Topical Conf. on RF Power in Plasmas, Moran, 2003, edit. C. Forest, AIP 694, 359
7. G. Taylor et al., Phys. Plasmas **12**, 052511 (2005)
8. P. Chattopadhyay et al., Phys. Plasmas **9**, No. 3 (2002)
9. F. Wagner et al., Phys. Rev. Lett. **49**, 1408 (1992)
10. F. Volpe, Electron Bernstein emission diagnostic of electron temperature profile at W7-AS Stellarator, PhD thesis, IPP Garching and Greifswald, IPP Report 13/1, March 2003 (124 pages)
11. F. Volpe, H.P.Laqua, Rev. Sci. Instrum. **74**, No. 3 (2003), pp. 1409-1413
12. A. Mueck et al., O-X-B Mode Conversion in the TCV Tokamak, Proc. 32nd EPS Conf. on Plasma Phys. and Contr. Fusion (Tarragona, 2005), P4.110
13. A. Mueck et al., Electron Bernstein Wave Heating in the TCV Tokamak, EC – 14, 14th Joint Workshop on Electron Cyclotron Emission and Electron Cyclotron Resonance Heating, Santorini, Greece, 2006
14. A. Mueck et al., Electron Bernstein Wave Heating in the TCV Tokamak, 47th Annual Meeting of the Division of Plasma Physics (Denver 2005), FP1.00062
15. A. Mueck et al., Electron Bernstein Wave Heating and Emission in the TCV Tokamak, Proc. 33nd EPS Conf. on Plasma Phys. and Contr. Fusion (Rome, 2006)
16. A. Manini, J.-M.Moret et al., Plasma Phys. Control. Fusion **44** (2002) 139-157
17. A. Sushkov, Y. Camenen, S. Coda, I. Klimanov, A. Pochelon, H. Weisen, Proc. 29th EPS Conference on Controlled Fusion and Plasma Physics, Montreux, Switzerland, June 2002, ECA Vol. **26B** (2002) P-4.118

Figure captions:

Figure 1: The ECRH system of TCV heats the plasma at the second harmonic with six gyrotrons at 82.7 GHz and a power of 500kW each. The waves are injected by four upper lateral launchers and two equatorial launchers which can be rotated in two directions.

Figure 2: Typical target plasma: high density ELMy H-mode with ELM-free phases. Modulated EC waves are injected in O-mode. When the plasma becomes overdense, the stray level is low in the ELM-free phases and increases in the ELMy phases, as shown in the highlighted region.

Figure 3: Normalized stray radiation power (violet) and D_α light emission (green). ELMs can strongly influence the stray radiation. The stray power, measured during the short EC pulses, rises from 30% to 80% during an ELMy phase.

Figure 4: Normalized stray radiation power vs. a) poloidal angle (with constant toroidal angle) and b) toroidal angle (with constant toroidal angle). The solid curves represent polynomial regression fits to the data points, the dashed lines represent 50% of the maximum stray level. A clear minimum in the stray radiation level is found for both angle scans.

Figure 5: Contour plot of calculated O-X conversion efficiency vs. launching angles. The innermost contour indicates 90% O-X conversion, the outermost 10%. The dashed lines denote the minimum and maximum angles of the 50% conversion window. The superimposed points give the angles of the experimental scans (see Figure 4). The green point corresponds to the extrapolated optimum experimental angles and is within 3° of the calculated angles.

Figure 6: Comparison of experimental (see Figure 4b) and simulated angular window. The experimental angular width is significantly broader than the simulated one, but can be explained by the finite width of the EC beam and the spread in its wave number spectrum.

Figure 6: Stray radiation for O- (violet) and X-mode (green) injection during an ELM-free period for identical injection angles and plasma conditions. In O-mode, the stray level is only about 40% of the stray level in X-mode.

Figure 7: Average deposited power from experiment with modulated EC wave injection, determined with the diamagnetic flux loop diagnostic. The absorbed power is about 60% of the injected EC power.

Figure 8: ART ray tracing calculation of the wave path in the a) poloidal and b) toroidal projections, including O-X-B double mode conversion.

Figure 9: The injection of modulated EC waves is visible directly on several radial soft X-ray time traces. To determine the deposition location, an FFT of each channel is performed.

Figure 10: a) Normalized FFT amplitude of the line-integrated soft X-ray time traces at the modulation frequency of the injected EC waves at 182 Hz vs. the chord number (green). The noise level is shown for reference (violet). b) Local soft X-ray emissivity oscillation amplitudes at the modulation frequency, derived by integral inversion from the line-integrated soft X-ray chords (green) and normalized density of the deposited beam power, calculated with ART. The power is absorbed well inside the cut-off at $\rho_\psi \sim 0.78$.

Figure 11: The long EC power pulses of 100 ms were injected to be able to show a temperature increase due to EBWH. A clear increase in the temperature, measured by

the soft X-ray absorber method is shown. The density remains essentially constant, which allows to attribute the temperature increase to EBWH (P_{Ohm} = 0.6 MW, P_{ECRH} = 1 MW and additional P_{ECRH} = 1 MW pulses of 100 ms).

Figure 12: Temperature profiles before the EC power pulse (1.0 s) and during the EC pulse (1.1 s), measured with Thomson scattering. The central temperature increase measured by Thomson scattering confirms the soft X-ray temperature measurement.

Figure 13: The emission at overdense conditions is measured at several frequencies. The onset of this emission varies with the density for the different frequencies, as expected. The onset densities correspond to the calculated cut-off densities within 5-10% for the various frequencies.

Figure 14: Comparison between calculated O-mode cut-off densities, the measured density from the FIR high time resolution line averaged density reconstruction and Thomson density measurement on axis for the square of several frequencies. A clear dependence with a deviation of less than 10% is shown.

Figure 15: Similar discharge as in Figure 14 but with a polarizer included to differ between opposite polarisation handinesses. The overdense emission signal is observed for only one handiness in ELM-free phases.